Journal of Inorganic Biochemistry 256 (2024) 112569

Contents lists available at ScienceDirect

Journal of Inorganic Biochemistry

journal homepage: www.elsevier.com/locate/jinorgbio

Navigating through the coordination preferences of heavy alkaline earth metals: Laying the foundations for ^{223}Ra- and $^{131/135m}$Ba-based targeted alpha therapy and theranostics of cancer

Sara Franchi [a], Andrea Madabeni [a], Marianna Tosato [b], Silvia Gentile [a], Mattia Asti [b], Laura Orian [a,c], Valerio Di Marco [a,*]

[a] Department of Chemical Sciences, University of Padova, 35131 Padova, Italy
[b] Radiopharmaceutical Chemistry Section, Nuclear Medicine Unit, AUSL-IRCCS Reggio Emilia, 42122 Reggio Emilia, Italy
[c] National Institute of Nuclear Physics, National Laboratories of Legnaro (INFN-LNL), 35020 Legnaro, Padova, Italy

ARTICLE INFO

Keywords:
Radium
Barium
Binding energy
Chelator
Energy decomposition analysis
Thermodynamics

ABSTRACT

The clinical success of [^{223}Ra]$RaCl_2$ (Xofigo®) for the palliative treatment of bone metastases in patients with prostate cancer has highlighted the therapeutic potential of α-particle emission. Expanding the applicability of radium-223 in Targeted Alpha Therapy of non-osseous tumors is followed up with significant interest, as it holds the potential to unveil novel treatment options in the comprehensive management of cancer. Moreover, the use of barium radionuclides, like barium-131 and -135m, is still unfamiliar in nuclear medicine applications, although they can be considered as radium-223 surrogates for imaging purposes. Enabling these applications requires the establishment of chelators able to form stable complexes with radium and barium radionuclides. Until now, only a limited number of ligands have been suggested and these molecules have been primarily inspired by existing structures known for their ability to complex large metal cations. However, a systematic inspection of chelators specifically tailored to Ra^{2+} and Ba^{2+} has yet to be conducted.

This work delves into a comprehensive investigation of a series of small organic ligands, aiming to unveil the coordination preferences of both radium-223 and barium-131/135m. Electronic binding energies of both metal cations to each ligand were theoretically computed *via* Density Functional Theory calculations (COSMO-ZORA-PBE-D3/TZ2P), while thermodynamic stability constants were experimentally determined for Ba^{2+}-ligand complexes by potentiometry, NMR and UV–Vis spectroscopies. The outcomes revealed malonate, 2-hydroxypyridine 1-oxide and picolinate as the most favorable building blocks to design multidentate chelators. These findings serve as foundation guidelines, propelling the development of cutting-edge radium-223- and barium-131/135m-based radiopharmaceuticals for Targeted Alpha Therapy and theranostics of cancer.

1. Introduction

Radium-223 (^{223}Ra) is an α-particle emitter characterized by a long half-life ($t_{1/2}$ = 11.4 d) and a massive energy release (27–28 MeV) that make it suitable for treatment of cancer [1–3]. During its decay, ^{223}Ra also emits γ-rays potentially useful for Single Photon Emission Computed Tomography (SPECT). However, the small photon abundance of suitable energy (< 2%) and the low activity injected in therapeutic assets produce quite low-quality images, so nowadays SPECT imaging with ^{223}Ra is mainly limited to the rough evaluation of activity biodistribution after therapy [2–6].

Barium-131 (^{131}Ba, $t_{1/2}$ = 11.5 d) and barium-135m (^{135m}Ba, $t_{1/2}$ =

Abbreviations: 1,2-HOPO, 2-Hydroxypyridine 1-oxide; 2,3-HOPO, 3-Hydroxy-2-pyridone; 3,4-HOPO, 3-Hydroxy-4-pyridone; ADF, Amsterdam Density Functional; COSMO, Conductor like Screening Model; DFT, Density Functional Theory; DMSO, Dimethyl sulfoxide; EDA, Energy Decomposition Analysis; EMA, European Medicines Agency; FDA, Food and Drug Administration; HOPO, Hydroxypyridone; HSAB, Hard and Soft Acids and Bases; NMR, Nuclear Magnetic Resonance; NOCV, Natural Orbitals for Chemical Valence; PBE, Perdew-Burke-Ernzerhof; SPECT, Single Photon Emission Computed Tomography; TAT, Targeted Alpha Therapy; TSP, 3-(Trimethylsilyl)propionic acid sodium salt; TZ2P, Triple-ζ with two sets of polarization functions; ZORA, Zeroth Order Regular Approximation.

* Corresponding author.
E-mail addresses: sara.franchi@phd.unipd.it (S. Franchi), andrea.madabeni@phd.unipd.it (A. Madabeni), marianna.tosato@ausl.re.it (M. Tosato), silvia.gentile@studenti.unipd.it (S. Gentile), mattia.asti@ausl.re.it (M. Asti), laura.orian@unipd.it (L. Orian), valerio.dimarco@unipd.it (V. Di Marco).

https://doi.org/10.1016/j.jinorgbio.2024.112569
Received 26 February 2024; Received in revised form 4 April 2024; Accepted 18 April 2024
Available online 23 April 2024

28.7 h) decay by electron capture and isomeric transition emitting 124 keV (30% abundance, together with higher energy radiations) and 268 keV (16%) γ-rays, respectively, and have been recently proposed as suitable ^{223}Ra surrogates for SPECT imaging due to the chemical similarity of these two metals. This would allow the so-called theranostic approach in cancer management [2,7,8].

The uniqueness of these alkaline earth radionuclides resides in their calcimimetic behavior: when injected *in vivo* as simple ionic compounds (*e.g.* $RaCl_2$), radioactive Ra^{2+} and Ba^{2+} cations spontaneously and selectively accumulate in the bone, thus making it possible to treat or image osseous diseases, including metastases [3,4,9,10]. Indeed, [^{223}Ra]$RaCl_2$ (Xofigo®) is currently used for the palliative treatment of bone metastases in adult patients with castration-resistant prostate cancer and it is the sole α-particle-emitting radiopharmaceutical authorized for clinical use by the U.S. Food and Drug Administration (FDA) and the European Medicines Agency (EMA) [4,11].

The successful application of [^{223}Ra]$RaCl_2$ in bone-related therapies, combined with the possible theranostic approach based on $^{131/135m}$Ba radionuclides, sparked interest in extending the use of ^{223}Ra to Targeted Alpha Therapy (TAT) of non-osseous tumors. However, to broaden the plethora of treatable tumors, the intrinsic propensity of Ra^{2+} and Ba^{2+} to accumulate in the bones must be prevented and the possibility to target new objectives should be enhanced. These issues can be circumvented by the stable incorporation of the metal cation into a system able to retain it *in vivo* and suitable to carry it to the target site [3,12]. One strategy, which is commonly employed for developing radiopharmaceuticals based on radioactive metals, is the bifunctional chelator approach, meaning that the radiometal is stably complexed by a chelator, in turn conjugated to a biologically active moiety able to direct the emitted radiation uniquely to the tumor expressing affinity for the biological vector. This strategy requires perfectly chemically-tailored chelators to fulfil the coordination requirements of the radiometal [13–16]. However, the shortage of chelating agents capable of firmly coordinating Ra^{2+} and Ba^{2+} *in vivo* has hindered their use in targeted cancer therapy and imaging to date. Indeed, very few chelators have been studied for the complexation of Ra^{2+} and Ba^{2+} for radiopharmaceutical applications. These include the macrocyclic ligands macropa and its larger counterpart macropa-XL, which provide two picolinic acid pendants attached to the two N atoms of a diaza-18-crown-6 and a diaza-21-crown-7 ring, respectively (Fig. 1) [12,17,18]. Macropa was investigated because it had previously shown a preference for large cations like La^{3+}, Ce^{3+}, Ac^{3+} and Ba^{2+} over smaller ones, and had been employed in lanthanum-132/135- and actinium-225-based radiopharmaceuticals [17,19–24]. Another proposed chelator is macrophospho, which bears two 2-pyridylphosphonic acid pendants on the same ring scaffold as that of macropa (Fig. 1) and which was studied for the complexation of Ba^{2+} [25]. Macrophospho was not originally conceived with a specific focus on Ba^{2+}, but its capability to complex this cation was explored due to its previously investigated positive behavior with the α-emitter bismuth-213 [15,26]. It is worth noting that both macropa and macrophospho were initially designed for different (radio)metals and later tested with Ra^{2+} or Ba^{2+}, adopting a "trial-and-observe" approach.

The structure of these three chelators involves a macrocyclic backbone functionalized with small chemical moieties provided with donor groups. The inclusion of side arms is crucial, since they both provide additional donors to the coordination sphere of the metal ion, thus increasing the inertness of the resulting complex, and increase the thermodynamic stability of the final complex. Although the use of picolinic and 2-pyridylphosphonic acid as pendants in macropa and macrophospho, respectively, provides encouraging outcomes regarding the feasibility of ^{223}Ra-based radiopharmaceuticals for TAT, and possibly of $^{131/135m}$Ba-labelled surrogates for diagnostic purposes, a systematic inspection of chemical groups expressly tailored to complex Ra^{2+} and Ba^{2+} is still an open field. This is likely because the fundamental coordination chemistry of Ba^{2+} and especially Ra^{2+} has not been explored to a large extent so far, hampering the rational design of proper binding platforms [3,27]. In fact, it is not easy to obtain thermodynamic information about radium complexes through standard techniques since all its isotopes are radioactive.

This work aims to investigate both *in silico* (for Ba^{2+} and Ra^{2+}) and experimentally (only for Ba^{2+}) the coordination preferences of these heavy alkaline earth metals in terms of binding affinity to a series of different donor atoms or groups. This exploration aims to lay the groundwork and provide the direction for the rational design and development of appropriate chelators to be employed in cutting-edge ^{223}Ra- and $^{131/135m}$Ba-based targeted radiopharmaceuticals. The structures of the molecules investigated in this study are listed in Fig. 2.

2. Materials and methods

2.1. Computational details

All Density Functional Theory (DFT) calculations were carried out with the Amsterdam Density Functional (ADF) 2019.307 program [28,29]. Geometry optimizations were performed with the Perdew-Burke-Ernzerhof (PBE) density functional, combined with the Grimme D3 dispersion correction and the original damping factor [30–32]. The TZ2P basis set (triple-ζ with two sets of polarization functions on each atom) with a small frozen core approximation was used for all atoms. Scalar relativistic effects were taken into account *via* the zeroth order regular approximation (ZORA), as implemented in ADF [33]. All calculations were performed in implicit solvent (water), with the Conductor like Screening Model (COSMO), employing the default ADF parameters for atomic radii, dielectric constant and definition of the molecular cavity [34,35]. Frequency calculations were performed to assess the true nature of all minima, for which only positive (real) frequencies were computed. Electronic binding energies (Δ*E*) for a plethora of monodentate and bidentate ligands to either "naked" (*i.e.*, not hydrated) or hydrated Ra^{2+} and Ba^{2+} were thus calculated at the COSMO-ZORA-PBE-D3/TZ2P level of theory [36]. This approach had been previously found to properly describe the geometric and thermodynamic features of heavy metals [36,37]. To obtain quantitative insight into metal-ligand bonding, selected complexes were investigated in the framework of the energy decomposition analysis (EDA) [37–41]. In EDA, the bonding energy (*i.e.*, the interaction energy between two

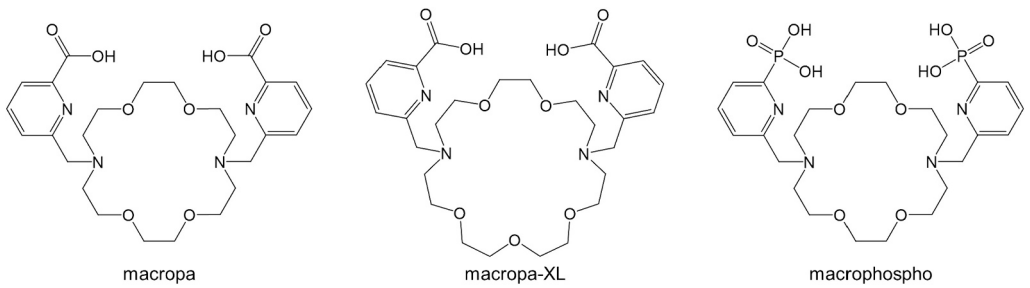

Fig. 1. Structures of macrocyclic chelators that have been recently proposed for Ba^{2+} and ^{223}Ra-based radiopharmaceuticals for TAT [12,17,18,25].

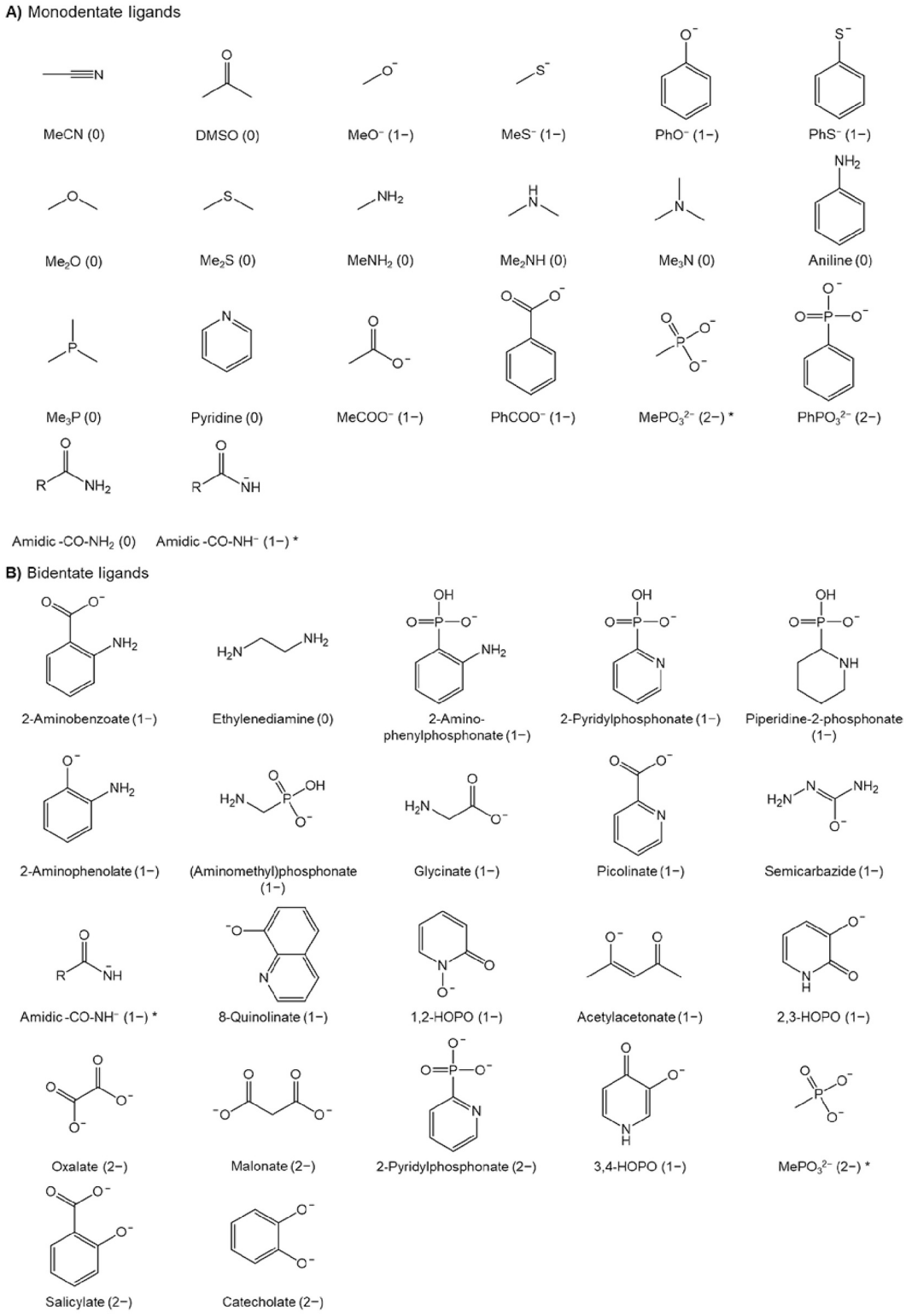

Fig. 2. Structures of A) monodentate and B) bidentate ligands that were investigated in this work (structures of H_2O and the halides are not shown). Their charge is in brackets. Only one resonance structure or tautomeric form is represented when more are possible. Ligands marked with an asterisk (*) were considered both as monodentate and as bidentate.

fragments – ΔE_{int}) was decomposed into chemically meaningful terms, *i.e.*, Pauli repulsion (ΔE_{Pauli}) accounting for two centers-four electrons repulsive interactions, orbital interaction (ΔE_{oi}) accounting for two centers-two electrons attractive interactions, electrostatic interaction (ΔV_{elst}), and ΔE_{disp} accounting for dispersive interactions (Eq. (1)).

$$\Delta E_{int} = \Delta E_{Pauli} + \Delta E_{oi} + \Delta V_{elst} + \Delta E_{disp} \quad (1)$$

Additionally, ΔE_{oi} was further decomposed into pairwise interactions *via* the Natural Orbitals for Chemical Valence (NOCV) partitioning method [42,43]. The NOCV are the eigenvectors of the

deformation density matrix ΔP. One important feature of the NOCV is to be paired in couples ($\varphi_{\pm k}$) with eigenvalues equal in absolute value, but with opposite sign ($\pm\nu_k$). These properties can be used to define a deformation density $\Delta\rho$ (*i.e.*, the change in molecular density after bond formation between the two fragments) according to the NOCV (Eq. (2)).

$$\Delta\rho = \sum_k \Delta\rho_k = \sum_k \nu_k\left(|\varphi_k|^2 - |\varphi_{-k}|^2\right) \quad (2)$$

The total orbital interaction term can thus be rewritten as the sum over pairwise contributions, each one associated to a NOCV pair and thus to a specific deformation density $\Delta\rho_k$ (Eq. (3)).

$$\Delta E_{oi} = \sum_k \Delta E_{oi}^k \quad (3)$$

Accordingly, this methodology allows the precise identification of the strongest orbital interactions, *i.e.*, those associated to the most stabilizing (most negative) ΔE_{oi}^k.

2.2. Thermodynamic experiments

A subset of representative ligands was further studied experimentally. All reagents were purchased from commercial suppliers (Sigma-Aldrich, Carlo Erba Reagents, Merck, Alfa Aesar, Prolabo, J.T. Baker, Riedal-De Haën, Carbosynth) and used as received. They were handled according to general safety practices adequate to chemistry laboratories. All experiments were performed in ultrapure water (18.2 MΩ/cm, from a Purelab Chorus Veolia system), unless otherwise stated, and at room temperature ($T = 25$ °C). Ionic strength (I) was not controlled due to the high amounts of Ba^{2+} salt required, which was introduced as $Ba(ClO_4)_2$ (Emsure).

2.2.1. NMR

Batch solutions containing a ligand at a fixed concentration ($C_L = 1{\cdot}10^{-2}$ M) and increasing amounts of $Ba(ClO_4)_2$ ($0 \le C_{Ba} \le 1$ M) were prepared in 90% H_2O + 10% D_2O. 3-(Trimethylsilyl)propionic acid sodium salt (TSP, Sigma-Aldrich, > 99%) was added to each solution as an internal standard for spectral calibration ($\delta = 0$ ppm). The pH of each solution was adjusted to an appropriate value by adding small aliquots (~ μL) of $HClO_4$ (Sigma-Aldrich) or CO_2-free NaOH (Emsure) solutions. pH was measured by using a Mettler Toledo SevenEasy pH-meter and a Crison (pH 0–14) combined glass electrode calibrated with commercial buffers at pH 4.01 and 7.00 (XS Instruments). Protonic Nuclear Magnetic Resonance (^{1}H NMR) spectra of each solution were acquired with a Bruker AMX 400 (400 MHz) spectrometer. Water signal was suppressed *via* the excitation sculpting pulse scheme.

2.2.2. UV–Vis

pH-Dependent in-cell titrations of the ligands and of solutions containing fixed amounts of ligand and $Ba(ClO_4)_2$ were performed ($C_L = 4{\cdot}10^{-4}$ M, $C_{Ba} = 4{\cdot}10^{-1}$ M for picolinic acid; $C_L = 6{\cdot}10^{-5}$ M, $C_{Ba} = 6{\cdot}10^{-3}$ M for 2-hydroxypyridine 1-oxide – 1,2-HOPO). The pH was adjusted and measured as described in *Paragraph 2.2.1*. UV–Vis spectra at different pH values were recorded in the wavelength range 200–800 nm with a Cary 60 spectrophotometer (Agilent) equipped with 1 cm optical path length quartz cuvettes.

2.2.3. Potentiometry

Automatic in-cell pH-potentiometric titrations of the ligands and of solutions containing fixed amounts of ligand and $Ba(ClO_4)_2$ were performed with NaOH ($C_L = 1{\cdot}10^{-3}$ or $1{\cdot}10^{-2}$ M, $C_{Ba} = 5{\cdot}10^{-2}$ M). Metrohm 715 Dosimat titrator and burets and a Metrohm 713 pH-meter were used. The pH was measured with a Hamilton (pH 0–14) combined glass electrode. The cell was thermostated by a water circulator at $T = 25$ °C and CO_2 was removed by bubbling purified N_2 before and during each measurement. A 0.1 M solution of HCl was prepared by dilution from the concentrated one (Aldrich, 37%) and standardized against Na_2CO_3 (Aldrich, 99.95–100.5%), which had been previously heated at 255–260 °C for 1 h to remove H_2O and CO_2. A CO_2-free 0.1 M solution of NaOH was standardized against the HCl solution and protected against carbonation.

A more detailed description of the potentiometric procedures was reported in our previous work [44].

2.2.4. Data treatment

NMR data (observed chemical shift – δ_{obs} – *vs* Ba^{2+}:L molar ratio – x) were fitted with SciDAVis software by using Eq. (4), which was obtained by solving a mathematical system of equations including the stability constants and the mass balances (Eqs. S1 – S4).

$$\delta_{obs} = \left\{\beta - \beta x - \frac{1}{C_L} + \left[\beta^2 x^2 + \left(\frac{2\beta}{C_L} - 2\beta^2\right)x + \beta^2 + \frac{1}{C_L^2} + \frac{2\beta}{C_L}\right]^{1/2}\right\} \bullet \frac{\delta_L - \delta_{BaL}}{2\beta} + \delta_{BaL} \quad (4)$$

In Eq. (4), β is the stability constant referred to the equilibrium $Ba^{2+} + L^{n-} \rightleftharpoons [BaL]^{(2-n)+}$, while δ_L and δ_{BaL} are the calculated chemical shifts of species L^{n-} (L denotes the general ligand and n− its charge) and $[BaL]^{(2-n)+}$, respectively. C_L was fixed as a constant parameter and not refined. UV–Vis and pH-potentiometric data were elaborated with HypSpec2014 and PITMAP programs [45,46], respectively. Conditional stability constants (β') were computed at pH = 7.4 and pH = 4 by multiplying β values by the coefficient α, which is the relative amount of ligand in its complexing form (L^{n-}) present at the pH of interest. Its value is $0 \le \alpha \le 1$ and depends on the ligand proton content. For example, for a monoprotic ligand having acidity constant K_a, Eq. (5) applies. The values of K_a for each ligand were taken from the literature and are collected in Table S1.

$$\alpha = \frac{1}{10^{pK_a - pH} + 1} \quad (5)$$

In all cases, the reported errors are standard deviations obtained from the fitting procedures and the propagation of error.

3. Results

3.1. Computational analysis

To assess Ra^{2+} and Ba^{2+} intrinsic ligand preferences, the electronic binding energies (ΔE) of "naked" Ra^{2+} and Ba^{2+} cations with a plethora of ligands were firstly computed *in silico* as described in *Paragraph 2.1*. The obtained results are shown in Tables 1–2.

Aiming at a more detailed description of Ra^{2+} donor preferences, and as further thermodynamic experiments are hampered by the radioactivity of all radium isotopes, the electronic reaction energy associated with the ligand exchange reaction between the Ra^{2+} *aquo*-complex ($[Ra(H_2O)_9]^{2+}$) [47] and an incoming monodentate ligand was also computed for representative ligands. The obtained data are summarized in Table S2, while the structures adopted for the *aquo*-complex and the complexes $[Ra(H_2O)_8(Me_3N)]^{2+}$, $[Ra(H_2O)_8(MeCOO)]^{+}$, and $[Ra(H_2O)_8(Me_2O)]^{2+}$ are reported in Fig. 3. The latter are shown as illustrative examples of the substitution of a water molecule in $[Ra(H_2O)_9]^{2+}$ by a monodentate ligand.

A quantitative bonding analysis was also performed for the Ra^{2+} complexes of selected monodentate ligands (*i.e.*, Me_2O, Me_2S, Me_3N, Me_3P, and $MeCOO^-$) within the framework of the EDA scheme (Table 3). Moreover, for the same ligands, the most important orbital interactions were identified by further decomposing the orbital interaction (ΔE_{oi}) term through the EDA-NOCV partitioning scheme (Table 3).

To further highlight the similarities between Ba^{2+} and Ra^{2+} coordination chemistry, the ligand exchange reaction energies between the Ba^{2+} *aquo*-complex ($[Ba(H_2O)_8]^{2+}$) and Me_2O, Me_2S, Me_3N, Me_3P were computed as well, and an EDA-NOCV analysis was performed for these

Table 1
Electronic binding energies (Δ*E*, kcal/mol) for monodentate ligands to "naked" Ra^{2+} and Ba^{2+} calculated in aqueous solution. Level of theory: COSMO-ZORA-PBE-D3/TZ2P.

Ligand (charge; donor)	Ra^{2+}	Ba^{2+}	Ligand (charge; donor)	Ra^{2+}	Ba^{2+}
H_2O (0; O)	−15.18	−14.89	$MeNH_2$ (0; N)	−20.58	−20.25
MeCN (0; N)	−15.79	−15.33	Me_2NH (0; N)	−19.78	−19.32
DMSO (0; O)	−23.42	−23.58	Me_3N (0; N)	−18.61	−17.97
Cl^- (1−; Cl)	−24.21	−23.79	Aniline (0; N)	−16.55	−15.60
Br^- (1−; Br)	−22.85	−22.23	Me_3P (0; P)	−16.88	−15.83
I^- (1−; I)	−21.55	−20.49	Pyridine (0; N)	−18.92	−18.54
MeO^- (1−; O)	−46.07	−47.92	$MeCOO^-$ (1−; O)	−30.27	−30.72
MeS^- (1−; S)	−29.53	−29.06	$PhCOO^-$ (1−; O)[a]	−28.68	−28.28
PhO^- (1−; O)	−36.13	−37.16	$MePO_3^{2-}$ (2−; O)[b]	−38.77	−39.72
PhS^- (1−; S)[a]	−29.09	−28.25	$PhPO_3^{2-}$ (2−; O)[a]	−41.73	−40.93
Me_2O (0; O)	−15.73	−15.38	Amidic -CO-NH_2 (0; O)	−22.44	−22.50
Me_2S (0; S)	−12.65	−11.67	Amidic -CO-NH^- (1−; N)[b]	−31.55	−31.51
			Amidic -CO-NH^- (1−; O)[b]	−33.38	−34.09

[a] The binding energy is partly due to π-cation interactions.
[b] These ligands were considered both as monodentate and as bidentate (see Table 2).

complexes (Table 4). The structure adopted for the *aquo*-complex of Ba^{2+} is reported in Fig. S1.

3.2. Thermodynamic experiments

For Ba^{2+}, a subset of monodentate and bidentate ligands, representative of various donor groups, were also explored experimentally through titrations followed by either NMR, UV–Vis or pH-potentiometry. One example of the obtained results for each technique is shown in Figs. 4–6, while the spectra, titrations and fitting curves for all the other investigated Ba^{2+}-ligand experiments are collected in the Supplementary Material (Figs. S2 – S12). The stability constants (both log*β* and log*β*') of $[BaL]^{(2-n)+}$ complexes were determined and are reported in Table S3. Their trends are also graphically shown in Fig. 7. When possible, the obtained results were compared to literature values, which were available only in a few cases (Table S3).

4. Discussion

4.1. Ra^{2+} and Ba^{2+} coordination preferences

Since all the isotopes of radium are highly radioactive, it is quite difficult to work with milligram amounts and millimolar concentrations of Ra^{2+} that are required to obtain thermodynamic data through standard techniques like potentiometry, NMR and UV–Vis spectroscopies. Consequently, barium is often used as a non-radioactive surrogate to explore the aqueous and coordination chemistry of radium, albeit this approach might be approximate in some cases [27,48–52]. Moreover, the study of ligands able to coordinate Ba^{2+} has also an intrinsic value, as two radionuclides (^{131}Ba and ^{135m}Ba) potentially useful for imaging

Table 3
EDA results (kcal/mol) for selected ligand-metal bond formations with the $[Ra(H_2O)_9]^{2+}$ *aquo*-ion. The Hirshfeld partial charge (*Q*) on the binding atom of the ligand is also reported in atomic units. The percentages are only relative to the stabilizing components of ΔE_{int}. Level of theory: ZORA-PBE-D3/TZ2P//COSMO-ZORA-PBE-D3/TZ2P.

	Me_2O	Me_2S	Me_3N	Me_3P	$MeCOO^-$
ΔE_r[a]	−2.32	−0.85	−5.46	−2.48	−8.89
ΔE_{int}	−23.35	−19.96	−27.13	−25.82	−179.43
ΔE_{Pauli}	17.83	16.67	24.71	22.7	35.54
ΔE_{oi}	−13.54 (32.8%)	−14.10 (38.5%)	−17.74 (34.2%)	−17.05 (35.1%)	−35.00 (16.3%)
ΔV_{elst}	−23.66 (57.4%)	−18.23 (49.8%)	−28.52 (55.0%)	−26.62 (54.9%)	−177.3 (82.4%)
ΔE_{disp}	−3.98	−4.3	−5.59	−4.85	−2.73
$\Delta E_{oi}^{(1)}$	−6.43	−8.76	−10.12	−11.12	−14.07
Q	−0.154	−0.018	−0.102	0.122	−0.469

[a] Level of theory: COSMO-ZORA-PBE-D3/TZ2P. ΔE_r values are taken from Table S2.

Table 2
Electronic binding energies (Δ*E*, kcal/mol) for bidentate ligands to "naked" Ra^{2+} and Ba^{2+} calculated in aqueous solution. Level of theory: COSMO-ZORA-PBE-D3/TZ2P.

Ligand (charge; donors)	Ra^{2+}	Ba^{2+}	Ligand (charge; donors)	Ra^{2+}	Ba^{2+}
2-Aminobenzoate (1−; N, O)	−35.30	−35.16	8-Quinolinate (1−; N, O)	−47.30	−47.59
Ethylenediamine (0; N, N)	−37.06	−36.54	1,2-HOPO (1−; O, O)	−47.47	−48.03
2-Amino-phenylphosphonate (1−; N, O)	−38.87	−38.46	Acetylacetonate (1−; O, O)	−47.87	−48.30
2-Pyridylphosphonate (1−; N, O)	−40.66	−40.44	2,3-HOPO (1−; O, O)[b]	−48.37	−48.81
Piperidine-2-phosphonate (1−; N, O)	−40.82	−40.07	Oxalate (2−; O, O)	−49.72	−50.28
2-Aminophenolate (1−; N, O)	−40.93	−41.38	Malonate (2−; O, O)	−49.86	−50.16
(Aminomethyl)phosphonate (1−; N, O)	−41.08	−40.77	2-Pyridylphosphonate (2−; N, O)	−50.22	−50.40
Glycinate (1−; N, O)	−41.75	−41.81	3,4-HOPO (1−; O, O)[c]	−51.56	−52.13
Picolinate (1−; N, O)	−42.27	−42.38	$MePO_3^{2-}$ (2−; O, O)[a]	−51.80	−52.08
Semicarbazide (1−; N, O)	−43.48	−43.76	Salicylate (2−; O, O)	−55.77	−56.56
Amidic -CO-NH^- (1−; N, O)[a]	−44.05	−43.69	Catecholate (2−; O, O)	−62.37	−63.40

[a] These ligands were considered both as monodentate and as bidentate (see Table 1).
[b] 2,3-HOPO is 3-hydroxy-2-pyridone.
[c] 3,4-HOPO is 3-hydroxy-4-pyridone.

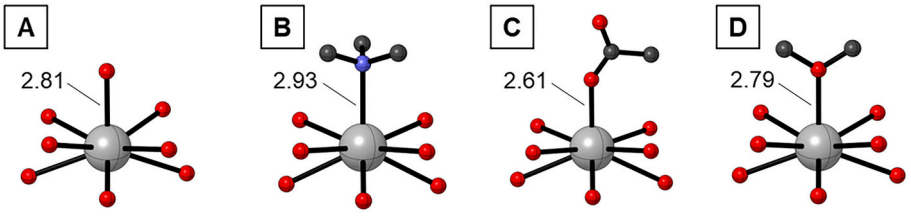

Fig. 3. Calculated geometries of A) $[Ra(H_2O)_9]^{2+}$ and of three illustrative complexes $[Ra(H_2O)_8L]^{(2-n)+}$ with B) L = Me_3N, C) L = $MeCOO^-$, and D) L = Me_2O. The Ra^{2+}-ligand bond length is displayed in Å. All hydrogen atoms have been hidden for clarity. Level of theory: COSMO-ZORA-PBE-D3/TZ2P.

Table 4
EDA results (kcal/mol) for selected ligand-metal bond formations with the $[Ba(H_2O)_8]^{2+}$ *aquo*-ion. The Hirshfeld partial charge (*Q*) on the binding atom of the ligand is the one reported in Table 3. The percentages are only relative to the stabilizing components of ΔE_{int}. Level of theory: ZORA-PBE-D3/TZ2P//COSMO-ZORA-PBE-D3/TZ2P.

	Me_2O	Me_2S	Me_3N	Me_3P
ΔE_r[a]	−1.89	−0.33	−5.36	−2.23
ΔE_{int}	−23.56	−19.91	−27.91	−25.46
ΔE_{Pauli}	16.58	16.11	24.06	22.30
ΔE_{oi}	−13.40 (33.4%)	−13.47 (37.4%)	−18.33 (35.3%)	−17.02 (35.6%)
ΔV_{elst}	−23.44 (58.4%)	−18.41 (51.1%)	−28.30 (54.4%)	−25.87 (54.2%)
ΔE_{disp}	−3.30	−4.14	−5.34	−4.87
$\Delta E_{oi}^{(1)}$	−6.05	−8.07	−10.48	−11.01

[a] Level of theory: COSMO-ZORA-PBE-D3/TZ2P.

purposes are available among its isotopes. For these reasons, we decided to screen a wide selection of ligands bearing different donor groups (O, S, N, P), and their combinations, *in silico* to compare their binding energies to Ra^{2+} and Ba^{2+}. Our computational approach encompasses a systematic analysis providing energetic information on Ra^{2+} and Ba^{2+} complexes with the monodentate and bidentate ligands depicted in Fig. 2. Then, a subset of the same ligands was further studied in experimental conditions to enhance our understanding of the thermodynamic stability of their Ba^{2+} complexes in aqueous solutions and so possibly acquaint the same information for Ra^{2+} with a reasonable degree of approximation.

4.1.1. *Computational investigation with monodentate ligands*

The binding energy (ΔE) of twenty-five different monodentate ligands (Fig. 2-A) was evaluated with the "naked" cations ($M^{2+} = Ra^{2+}$ or Ba^{2+}), according to the reaction Eq. (6) and including solvation with a continuum dielectric model.

$$M^{2+} + L^{n-} \rightarrow [ML]^{(2-n)+} \quad (6)$$

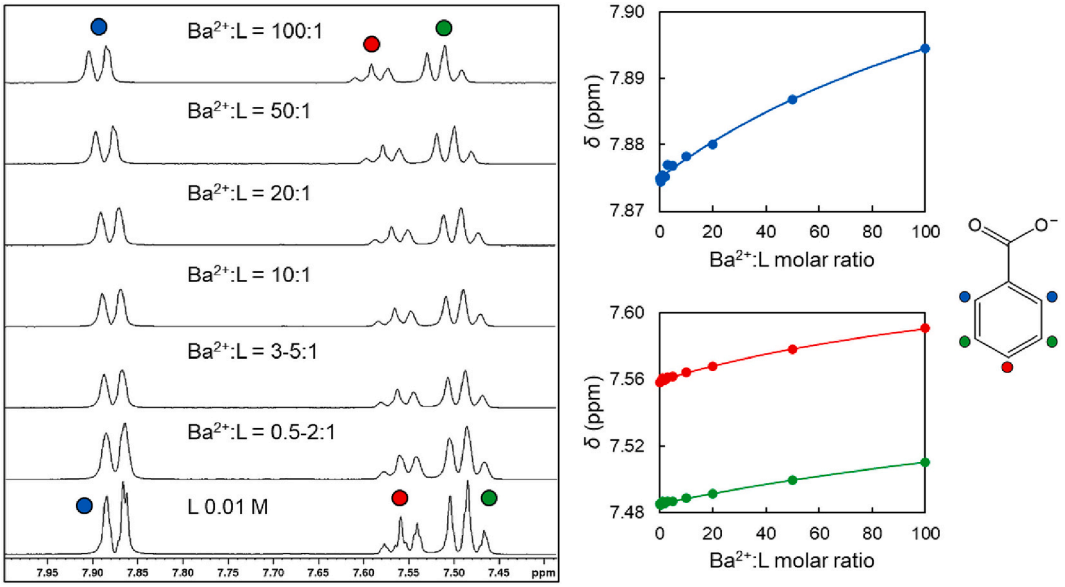

Fig. 4. ^1H NMR spectra of Ba^{2+}-L solutions (L = benzoate) recorded at increasing Ba^{2+}:L molar ratios at pH 10.4–11.8 (left) and data fitting (middle). Signal attribution is represented on the right.

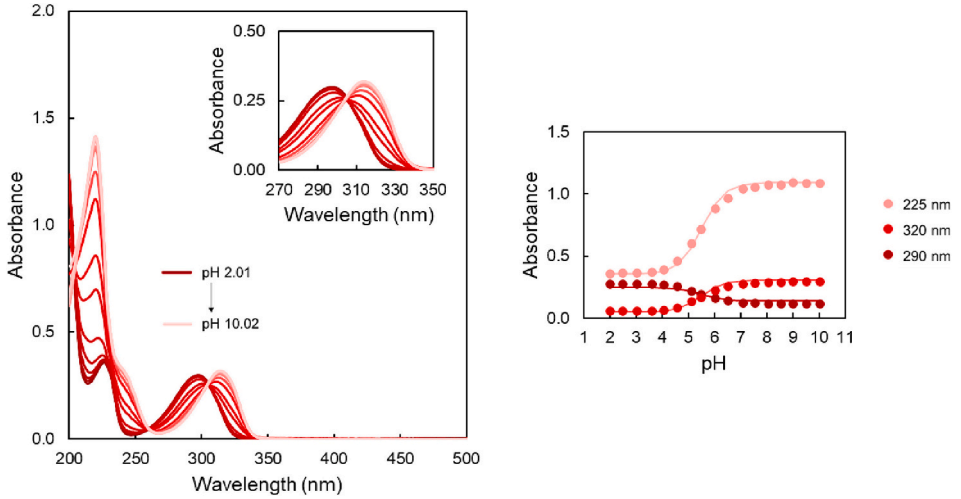

Fig. 5. UV–Vis spectra of Ba^{2+}-L solutions (L = 1,2-HOPO, $C_L = 6{\cdot}10^{-5}$ M, $C_{Ba} = 6{\cdot}10^{-3}$ M) recorded at increasing pH (left) and data fitting at selected wavelengths (right).

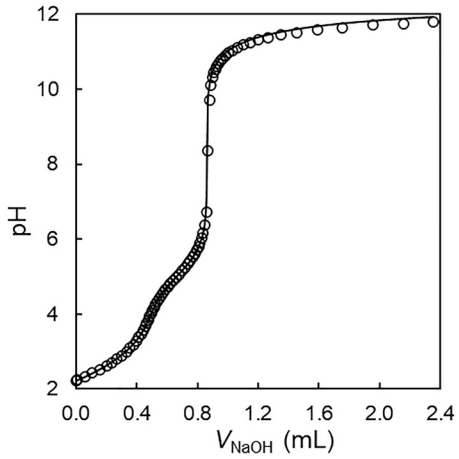

Fig. 6. Curve of a potentiometric titration of a Ba^{2+}-L solution (L = malonate, $C_L = 1{\cdot}10^{-2}$ M, $C_{Ba} = 5{\cdot}10^{-2}$ M) with a solution of 0.1 M NaOH.

This approach can be expected to underestimate the solvation of charged species, especially the metal cation, nevertheless it provides a close-up on the intrinsic trends in the strength of metal-ligand bonds. The results reported in Table 1 immediately disclose that no great difference is appreciable when comparing Ra^{2+} to Ba^{2+}, as far as the intrinsic strength of the metal-ligand bond is concerned. Indeed, only differences of fractions of kcal/mol are predicted when the two metals bind to the same ligand. While this quantitative result is affected by the lack of explicit solvation, it suggests that Ba^{2+} coordination chemistry closely resembles that of Ra^{2+}, thus validating its use in the explorative investigations of the radioactive element.

Among the plethora of the investigated ligands, both Ra^{2+} and Ba^{2+} display preferences for those defined as hard species, according to Pearson's Hard and Soft Acids and Bases (HSAB) theory [53]. For instance, oxygen-based ligands (*e.g.*, Me_2O, MeO^- and PhO^-) form stronger bonds (*i.e.*, more negative ΔE) than their softer sulfur-based counterparts (*e.g.*, Me_2S, MeS^-, PhS^-). Similarly, trimethylamine (Me_3N) binds more strongly to both metals than trimethylphosphine (Me_3P).

In addition, increasing the charge of the ligand leads to stronger binding energies, as can be inferred by comparing mono-anionic (*e.g.*, $MeCOO^-$ and $PhCOO^-$) to bis-anionic oxygen-based ligands (*e.g.*, $MePO_3^{2-}$ and $PhPO_3^{2-}$). Among the neutral ligands, amines (*e.g.*, Me_3N) appear to bind Ra^{2+} and Ba^{2+} moderately better than ethers (Me_2O) (ΔE difference = −2.6-2.8 kcal/mol). This outcome, which is apparently in opposition to the HSAB theory, was further explored through EDA, as discussed in *Paragraph 4.2*.

The subsequent assessment was extended to exchange reactions involving ligands and $[M(H_2O)_x]^{2+}$, aimed to better simulate solution conditions (Eq. (7)). These calculations were carried out mainly for Ra^{2+}, as information about Ba^{2+} chemistry can also be obtained from experimental data. Selected ligand exchange reactions (*i.e.*, with Me_2O, Me_2S, Me_3N, and Me_3P) were also computed for Ba^{2+} to verify whether the similarity between the coordination chemistry of the two metals holds true in the presence of explicit solvation as well.

$$\left[Ra(H_2O)_9\right]^{2+} + L^{n-} \rightarrow \left[Ra(H_2O)_8L\right]^{(2-n)+} + H_2O \quad (7)$$

$$\left[Ba(H_2O)_8\right]^{2+} + L^{n-} \rightarrow \left[Ba(H_2O)_7L\right]^{(2-n)+} + H_2O$$

In the ligand exchange reaction, one water molecule is expelled and replaced in the coordination sphere of M^{2+} by the incoming ligand. This reaction was chosen to mimic more closely the solution conditions, where the "naked" Ra^{2+}/Ba^{2+} is not the representative species. The chosen species of Ra^{2+} *aquo*-complex was $[Ra(H_2O)_9]^{2+}$, since a recent study highlighted a coordination number of 9 for the hydrated radium cation [47]. It is worth underlining that different starting geometries have been considered, but in all cases, at our level of theory, the fully converged geometry is a capped square antiprismatic arrangement (Fig. 3-A). Since the nine-coordinated arrangement of Ra^{2+} is deemed to be highly labile in solution [47], it is likely that other arrangements might be feasible as well. However, we do not envision that a different coordination arrangement could strongly affect the trends in the ligand exchange reaction energy shown in Table S2. Starting from this arrangement, the apical (*i.e.*, capping) water molecule was substituted by each of the investigated ligands (*e.g.*, Fig. 3-B, C, D).

As for Ba^{2+}, recent experimental and theoretical evidences agree on

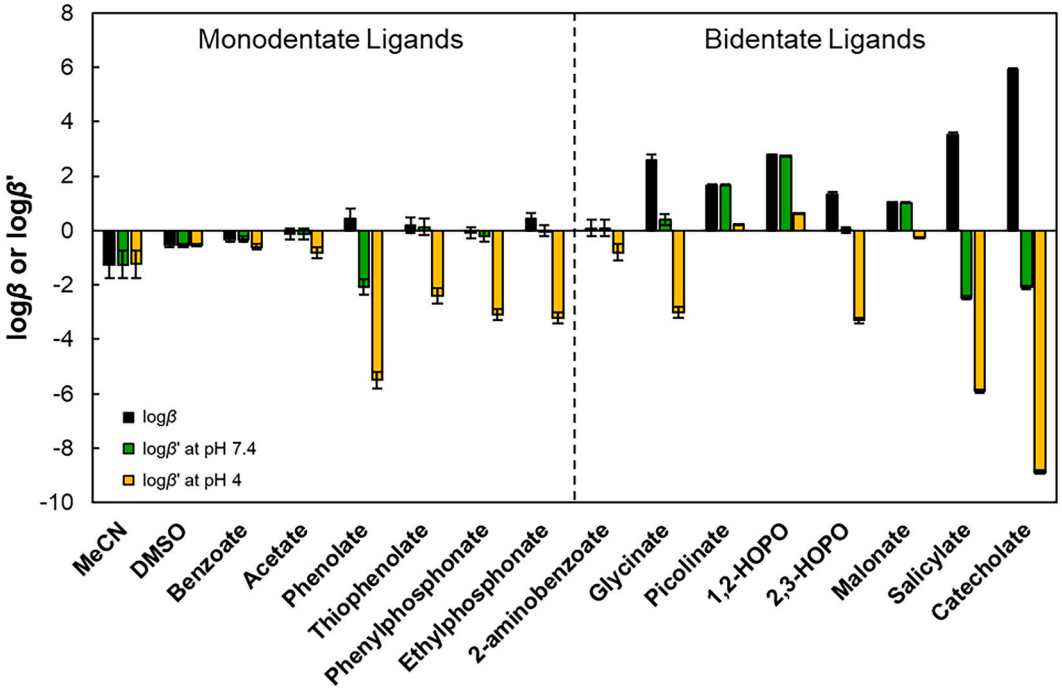

Fig. 7. Thermodynamic (logβ) and conditional (logβ') stability constants of $[BaL]^{(2-n)+}$ complexes. Logβ' were calculated at pH 7.4 and 4.

an average coordination number of 8 for the first solvation shell around the metal ion [54,55]. In this case the solvation shell is deemed to be labile as well, thus different geometries and arrangements exist in solution. In our case, various attempts converged to a distorted bicapped trigonal prism or distorted square antiprismatic geometry for $[Ba(H_2O)_8]^{2+}$ (Fig. S1), which was used as the reactant in the ligand exchange reactions. One water molecule was substituted in turn by each incoming ligand. The geometry of substituted complexes $[Ba(H_2O)_7L]^{(2-n)+}$ is not shown since it is not well defined, and it slightly changes for different ligands.

In all cases, as expected, the ligand exchange reaction displays a less negative reaction energy (ΔE_r) than the corresponding binding energy (ΔE). This occurs because the first explicit solvation shell around M^{2+} dampens the electrostatic interaction between the metal and the ligand (Table S2 *vs* Table 1). Nevertheless, the qualitative conclusions discussed for the "naked" metal ions persist within this more elaborate model and are further supported by the trend of ΔE_r. In particular, the preference of Ra^{2+} for hard ligands remains evident. Similarly, charged oxygen-based ligands are characterized by the most negative ΔE_r. However, some distinctions emerge. For instance, while the halides (Cl^-, Br^- and I^-) appear to bind Ra^{2+} more strongly than amines within the "naked"-ion model, their ligand exchange reaction involving the *aquo*-ion suggests a different scenario. In the latter case, their ΔE_r are quite close to those of amines, revealing a similar binding affinity to the Ra^{2+} (and likely Ba^{2+}) solvated cation. The computed ligand exchange reaction energies for $[Ba(H_2O)_8]^{2+}$ highlight that the coordination chemistry of barium with Me_2O, Me_2S, Me_3N and Me_3P closely matches that of radium also when the explicitly solvated metal is considered. Indeed, almost identical reaction energies were computed (Table 4 *vs* Table S2).

4.1.2. Computational investigation with bidentate ligands

A series of twenty-two bidentate ligands (Fig. 2-B), varying in charges (0, −1, −2) and donor atoms (oxygen and nitrogen), was also tested, employing the model depicted in Eq. (6), excluding the explicit solvation of the metal cation (Table 2). The qualitative conclusions described for the monodentate ligands hold true for this series as well. Specifically, more negatively charged hard ligands exhibit stronger bindings to both Ra^{2+} and Ba^{2+}. Importantly, and in analogy with monodentate ligands, no strong differences between Ra^{2+} and Ba^{2+} emerged.

4.1.3. Experimental investigation with mono and bidentate ligands

Following the *in-silico* screening of the ligand set, our subsequent phase involved experimental investigations into the thermodynamic stability of Ba^{2+} complexes in aqueous solutions, utilizing a representative selection of monodentate and bidentate ligands. The titrations of a fixed amount of ligand with increasing $Ba(ClO_4)_2$ at constant pH were followed *via* NMR spectroscopy to observe the variation of non-exchangeable protons' chemical shift (δ) with Ba^{2+} concentration. The trend of δ as a function of Ba^{2+}:ligand molar ratio for each ^1H nucleus is a curve that starts at the value δ_L representing the free ligand, and reaches a plateau when the formation of $[BaL]^{(2-n)+}$ is complete (δ_{BaL}). The data can be fitted with Eq. (4) to obtain the stability constant of $[BaL]^{(2-n)+}$ complex (logβ). The equation requires the assumption of a speciation model (*i.e.*, number and stoichiometry of the complexes present at equilibrium) before the calculation is performed. In our conditions, it is reasonable to assume that $[BaL]^{(2-n)+}$ is the only one or the predominant species by far. In fact, due to the large molar excess of Ba^{2+} with respect to L^{n-} used in the experiments (*i.e.*, Ba^{2+} concentration reached up to 100-fold that of L^{n-} at the end of each titration), it is unlikely that complexes with more than one ligand bound to one Ba^{2+} cation (*e.g.*, $[BaL_2]^{(2-2n)+}$, $[BaL_3]^{(2-3n)+}$) occurred. Such high Ba^{2+} concentrations were crucial to promote complex formation due to the relatively low thermodynamic stability of the investigated complexes. On the other hand, complexes with more than one Ba^{2+} bound to a single ligand molecule (*e.g.*, $[Ba_2L]^{(4-n)+}$, $[Ba_3L]^{(6-n)+}$) are very unlikely as well, since we dealt with mono or short bidentate ligands that very hardly could act as a bridge between two metal centers.

For specific ligands (*i.e.*, picolinate, 1,2-HOPO, 2,3-HOPO, malonate, salicylate, and catecholate), pH-dependent titrations of fixed amounts of ligand and $Ba(ClO_4)_2$ were conducted *via* UV–Vis or potentiometry, thanks to the higher stability of their complexes with respect to the other ligands. In these cases, either the trend of the absorbance at selected wavelengths *vs* pH, or the trend of the measured pH *vs* the added amount of base, can be fitted with appropriate softwares to determine logβ. Relatively high barium-to-ligand molar ratios (5- to 1000-fold) were employed in these cases too to promote the complexation.

The logβ found in this work reasonably match those available in literature. The agreement can be considered satisfactory also considering the relatively high uncertainties arising from the quite low stability of the complexes (Table S3).

Since logβ represent the experimental thermodynamic stability of Ba^{2+} complexes, their values can be compared to the computed binding energies for $[BaL]^{(2-n)+}$, even if a rigorous comparison would require to take into account entropic contributions as well, which are not considered within the calculation of ΔE. Within this approximation, a quite good linear correlation ($R^2 = 0.77$) is observed when plotting logβ as a function of ΔE (Fig. 8). The correlation points out a satisfactory agreement between the trend of logβ and the trend of theoretical ΔE across all the investigated ligands. These results highlight that the strongest binding interactions and thus the most stable Ba^{2+} complexes (*i.e.*, higher logβ), and with a good approximation also Ra^{2+} complexes, are formed with bidentate ligands containing negatively charged, hard donor groups, particularly those with oxygen as donor atoms, such as phosphonates, carboxylates, alkyl and aryl oxides. Deprotonated picolinic and 2-pyridylphosphonic acids may be taken as reference ligands since they are the building blocks of macropa, macropa-XL and macrophospho (Fig. 1). They appear as very good candidates for the complexation of Ra^{2+} and Ba^{2+}. However, ligands with more oxygen donors, such as hydroxypyridones (HOPOs), dicarboxylic acids like malonic acid, dihydroxide derivatives like catechol, and hybrids like salicylic acid, may surpass their stability.

Lastly, conditional stability constants (logβ') at pH 7.4 and 4 were calculated to take into account how the thermodynamic stability of the ligand-metal complex is influenced by the protonation state of the ligand (based on its pK_a) at radiochemically relevant pH (Table S3 and Fig. 7). In fact, solutions for the radiolabeling of radiopharmaceuticals are commonly buffered at pH values between 4 and 7.4 [17,18], and additionally the latter is the physiological pH: under these conditions, proton competition may lower the effective stability of the complexes. Logβ' has the same value as logβ if the ligand is fully deprotonated at the pH of interest, while it decreases as a function of the protonation state according to the basicity of the ligand as H^+ can compete with the complexation of Ba^{2+} (or Ra^{2+}). Therefore, while logβ (and the corresponding computed ΔE) represents the thermodynamic affinity between ligand and metal, logβ' values express the effective stability of the metal complexes at a given pH. If logβ' values are considered, 1,2-HOPO, picolinate, and malonate emerge as the most promising Ba^{2+}/Ra^{2+} binding moieties.

4.2. On the origin of Ra^{2+} and Ba^{2+} preference for hard donors

To understand the origin of Ra^{2+} and Ba^{2+} pronounced preference for hard donors, a quantitative bonding analysis was performed on the complexes of selected monodentate ligands within the framework of the EDA scheme (Tables 3–4). Particularly, Me_2O was compared to Me_2S and Me_3N to Me_3P. For Ra^{2+} EDA was also performed on $MeCOO^-$ as a representative charged ligand, to account for the effect of charge on the binding energy. It must be pointed out that in the EDA framework the solvation effect is not conventionally considered. Thus, this analysis was performed as gas phase single point energy calculations on the geometries optimized in water. This approach had been previously used in the

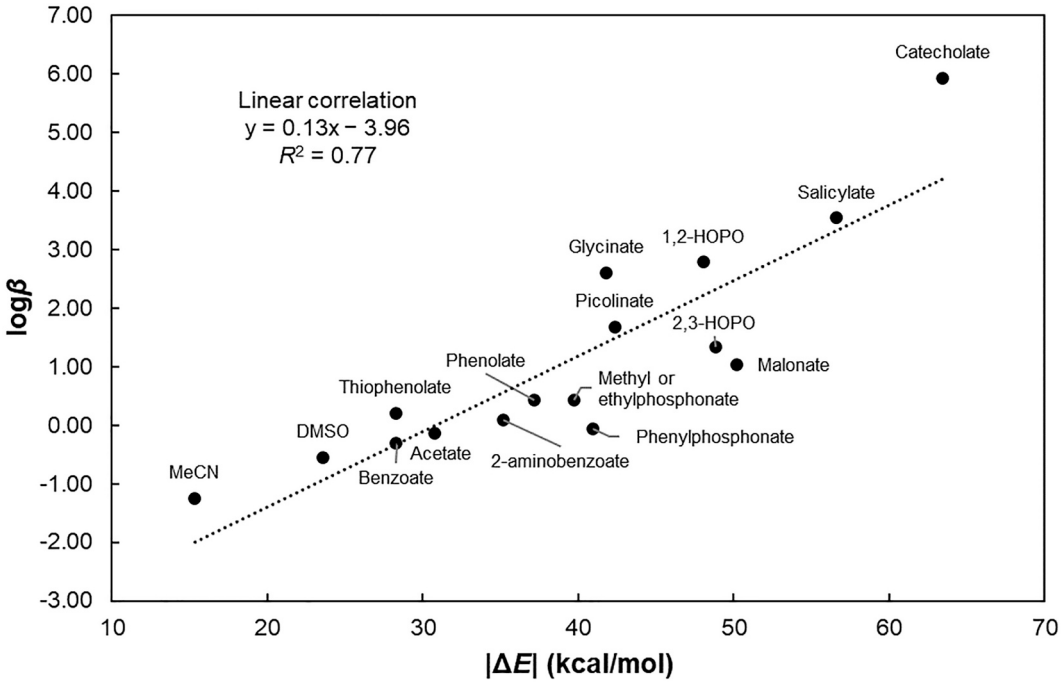

Fig. 8. Correlation between the calculated electronic binding energies (their absolute value $|\Delta E|$ is reported, kcal/mol) and the thermodynamic stability constants ($\log\beta$) of Ba^{2+} complexes. Only the ligands for which both the computational and experimental investigations were carried out are shown. Level of theory: COSMO-ZORA-PBE-D3/TZ2P.

literature to obtain a qualitative insight into ligand preferences for charged heavy metals [36,37]. To obtain the most representative description at our current level of theory, the metal-ligand interaction was investigated between radium/barium and the selected ligands (L) in the *aquo*-complexes $[Ra(H_2O)_8L]^{(2-n)+}$ and $[Ba(H_2O)_7L]^{(2-n)+}$.

The observed trends in ΔE_r align with those in ΔE_{int}, emphasizing that the most favored ligand exchanges are due to the formation of the strongest ligand-metal interactions. Across all cases, ΔV_{elst} term is consistently the strongest contribution to ligand-metal bonding, regardless of the atoms involved. Indeed, for all tested cases, ΔV_{elst} accounts for ~50–60% of the overall stabilizing interaction. Conversely, ΔE_{oi} accounts for ~30–40% of the stabilization. These results are consistent with a predominantly ionic bond which however includes also important covalent contributions. Accordingly, the two harder ligands (*i.e.*, Me_2O and Me_3N) display a more stabilizing electrostatic contribution than their softer counterparts (*i.e.*, Me_2S and Me_3P, respectively). Thus, the preference of Ra^{2+} and Ba^{2+} for hard ligands appears to be mainly due to electrostatic factors. This result is in line with the qualitative trend of the Hirshfeld partial charges on the donor atom (Table 3). Indeed, the partial charge on oxygen is more negative than the sulfur one, and the partial charge on nitrogen is more negative than the phosphorus one. Interestingly, the stronger bond between Ra^{2+}/Ba^{2+} and Me_3N with respect to Me_2O is also characterized by a stronger electrostatic interaction, despite oxygen having a more negative partial charge than nitrogen. A careful inspection of the electrostatic potential reveals that, despite the less negative partial charge, the nitrogen atom in Me_3N has a more localized negative potential, while the potential is more evenly spread over oxygen in Me_2O (Fig. 9). This different feature accounts for the stronger Ra-N (and Ba-N) bond with respect to the Ra-O (and Ba-O) one. Additionally, ΔE_{oi} and ΔE_{disp} are also more stabilizing for Me_3N with respect to Me_2O.

Although orbital interaction only plays a secondary role in bond stability, the most significant covalent interaction was quantified through the EDA-NOCV partitioning scheme. Expectedly, in all cases the most important covalent contribution to the metal-ligand bond comes from the σ-donation of the ligand to the metal ($\Delta E_{oi}^{(1)}$). This term is systematically associated to the single strongest contribution to each ΔE_{oi} and to the strongest NOCV eigenvalue (ν_k) (*i.e.*, to the most intense ligand-to-metal charge transfer). The absolute value of $\Delta E_{oi}^{(1)}$ increases from Me_2O to Me_2S and from Me_3N to Me_3P, suggesting a stronger σ-donation capability towards Ra^{2+} and Ba^{2+} by the softer ligands. Nevertheless, the combined effect of all $\Delta E_{oi}^{(n)}$ results in only small differences between the overall ΔE_{oi} of harder and softer analogous ligands. Additionally, the stronger σ-donation of Me_3N with respect to Me_2O partially contributes to its stronger binding to both metals.

Lastly, as expected, the EDA for the charged $MeCOO^-$ ligand shows a very negative ΔE_{int}, due to the strong effect of ΔV_{elst}, which almost perfectly matches the value of the interaction. While this effect is very likely overestimated due to the lack of implicit solvation, it reinforces the concept of the importance of the electrostatic contribution to Ra-L bond formation.

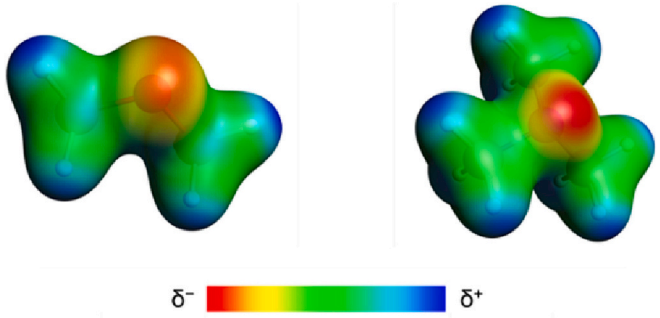

Fig. 9. Molecular electrostatic potential over Me_2O (left) and Me_3N (right). Red areas correspond to a negative electrostatic potential, while blue areas correspond to a positive electrostatic potential. (For interpretation of the references to color in this figure legend, the reader is refered to the web version of this article.)

5. Conclusions

The use of ^{223}Ra in nuclear medicine is the current state of the art of α-particle therapy but is limited to the treatment of prostate-cancer-derived bone metastases so far. The possibility to extend ^{223}Ra employment also to TAT of non-osseous tumors is very appealing but still challenging, due to the absence of a carrier system able to stably incorporate and retain this metal *in vivo*. On the other hand, the use of barium radionuclides such as ^{131}Ba and ^{135m}Ba is still unfamiliar in nuclear medicine applications, although their utilization could be postulated as ^{223}Ra surrogates for imaging purposes. The development of chemically tailored chelators suitable for the complexation of Ra^{2+} and Ba^{2+} *in vivo* represents an unexplored area, also constrained by the limited knowledge on Ra^{2+} coordination preferences due the radioactivity of all its isotopes. In this work, a plethora of monodentate and bidentate ligands, which are possible candidates as pendants in macrocyclic chelators suitable to strongly complex Ra^{2+} or Ba^{2+}, were considered, and their interaction with both Ra^{2+} and Ba^{2+} was investigated theoretically and experimentally. Electronic binding energies of each ligand to Ra^{2+} and Ba^{2+} were calculated using a relativistic DFT-based protocol, while stability constants were determined for Ba^{2+} through a combination of thermodynamic techniques. Both approaches converged to reveal that these heavy alkaline earth metal cations form stronger interactions with ligands possessing negative charges and exhibiting hard donor characteristics, particularly those involving oxygen atoms. Notably, 1,2-HOPO, picolinate, and malonate emerged as the most promising candidates. Moreover, quantitative bonding analyses highlighted the pivotal role of electrostatic interactions in Ra^{2+} and Ba^{2+} preference for hard donors, with covalent contributions only moderately influencing bonding stability.

These findings hold promise in guiding the strategic design of chelators specifically tailored to meet the chemical requirements of Ra^{2+} and Ba^{2+}, potentially paving the way for groundbreaking novel targeted ^{223}Ra/$^{131/135m}$Ba theranostic radiopharmaceuticals. This insight could significantly advance the development of novel therapies in nuclear medicine, extending the scope of these radiometals beyond their current applications.

Funding

This research did not receive any specific grant from funding agencies in the public, commercial, or not-for-profit sectors.

CRediT authorship contribution statement

Sara Franchi: Conceptualization, Data curation, Formal analysis, Investigation, Methodology, Project administration, Visualization, Writing – original draft, Writing – review & editing. **Andrea Madabeni:** Data curation, Investigation, Methodology, Writing – original draft. **Marianna Tosato:** Conceptualization, Writing – review & editing. **Silvia Gentile:** Investigation. **Mattia Asti:** Writing – review & editing. **Laura Orian:** Resources, Supervision, Writing – review & editing. **Valerio Di Marco:** Resources, Supervision, Writing – review & editing.

Declaration of competing interest

The authors have no competing interests to declare.

Data availability

Data will be made available on request.

Acknowledgements

The Italian National Institute of Nuclear Physics (INFN) has generously provided computational resources (Cloud Veneto) for the theoretical investigation. CINECA (Casalecchio del Reno, IT) is also kindly acknowledged for the access to their infrastructures (HPC cloud) through the project DIRAC-1 (PI: L.O.).

Appendix A. Supplementary data

Supplementary data to this article can be found online at https://doi.org/10.1016/j.jinorgbio.2024.112569.

References

[1] M.G. Ferrier, V. Radchenko, An appendix of radionuclides used in targeted alpha therapy, J. Med. Imag. Radiat. Sci. 50 (2019) S58–S65, https://doi.org/10.1016/j.jmir.2019.06.051.
[2] IAEA Nuclear Data Section. https://www-nds.iaea.org/.
[3] S. Franchi, M. Asti, V. Di Marco, M. Tosato, The Curies' element: state of the art and perspectives on the use of radium in nuclear medicine, EJNMMI Radiopharm. Chem. 8 (2023), https://doi.org/10.1186/s41181-023-00220-4.
[4] T.D. Poeppel, D. Handkiewicz-Junak, M. Andreeff, A. Becherer, A. Bockisch, E. Fricke, L. Geworski, A. Heinzel, B.J. Krause, T. Krause, M. Mitterhauser, W. Sonnenschein, L. Bodei, R.C. Delgado-Bolton, M. Gabriel, EANM guideline for radionuclide therapy with radium-223 of metastatic castration-resistant prostate cancer, Eur. J. Nucl. Med. Mol. Imaging 45 (2018) 824–845, https://doi.org/10.1007/s00259-017-3900-4.
[5] D.S. Abou, A. Rittenbach, R.E. Tomlinson, P.A. Finley, B. Tsui, B.W. Simons, A. K. Jha, D. Ulmert, R.C. Riddle, D.L.J. Thorek, Preclinical single photon emission computed tomography of alpha particle-emitting radium-223, Cancer Biother. Radiopharm. 35 (2020) 520–529, https://doi.org/10.1089/cbr.2019.3308.
[6] N. Herrero Álvarez, D. Bauer, J. Hernández-Gil, J.S. Lewis, Recent advances in radiometals for combined imaging and therapy in cancer, ChemMedChem 16 (2021) 2909–2941, https://doi.org/10.1002/cmdc.202100135.
[7] F. Reissig, D. Bauer, M. Ullrich, M. Kreller, J. Pietzsch, C. Mamat, K. Kopka, H. J. Pietzsch, M. Walther, Recent Insights in Barium-131 as a Diagnostic Match for Radium-223: Cyclotron Production, Separation, Radiolabeling, and Imaging, Pharmaceuticals 13, 2020, pp. 1–16, https://doi.org/10.3390/ph13100272.
[8] F. Reissig, K. Kopka, C. Mamat, The impact of barium isotopes in radiopharmacy and nuclear medicine – from past to presence, Nucl. Med. Biol. 98 (2021) 59–68, https://doi.org/10.1016/j.nucmedbio.2021.05.003.
[9] S. Poty, L.C. Francesconi, M.R. McDevitt, M.J. Morris, J.S. Lewis, α-Emitters for radiotherapy: from basic radiochemistry to clinical studies—part 1, J. Nucl. Med. 59 (2018) 878–884, https://doi.org/10.2967/jnumed.116.186338.
[10] N.D. Priest, L.T. Dauer, D.G. Hoel, Administration of lower doses of radium-224 to ankylosing spondylitis patients results in no evidence of significant overall detriment, PLoS One 15 (2020) 1–10, https://doi.org/10.1371/journal.pone.0232597.
[11] M. Makvandi, E. Dupis, J.W. Engle, F.M. Nortier, M.E. Fassbender, S. Simon, E. R. Birnbaum, R.W. Atcher, K.D. John, O. Rixe, J.P. Norenberg, Alpha-emitters and targeted alpha therapy in oncology: from basic science to clinical investigations, Target. Oncol. 13 (2018) 189–203.
[12] A.S. Ivanov, M.E. Simms, V.S. Bryantsev, P.D. Benny, J.R. Griswold, L.H. Delmau, N.A. Thiele, Elucidating the coordination chemistry of the radium ion for targeted alpha therapy, Chem. Commun. 58 (2022) 9938–9941, https://doi.org/10.1039/d2cc03156f.
[13] E. Boros, A.B. Packard, Radioactive transition metals for imaging and therapy, Chem. Rev. 119 (2019) 870–901.
[14] E.W. Price, C. Orvig, Matching chelators to radiometals for radiopharmaceuticals, Chem. Soc. Rev. 43 (2014) 260–290.
[15] S. Franchi, V. Di Marco, M. Tosato, Bismuth chelation for targeted alpha therapy: current state of the art, Nucl. Med. Biol. 114–115 (2022) 168–188, https://doi.org/10.1016/j.nucmedbio.2022.06.002.
[16] T.I. Kostelnik, C. Orvig, Radioactive main group and rare earth metals for imaging and therapy, Chem. Rev. 119 (2019) 902–956.
[17] D.S. Abou, N.A. Thiele, N.T. Gutsche, A. Villmer, H. Zhang, J.J. Woods, K. E. Baidoo, F.E. Escorcia, J.J. Wilson, D.L.J. Thorek, Towards the stable chelation of radium for biomedical applications with an 18-membered macrocyclic ligand, Chem. Sci. 12 (2021) 3733–3742, https://doi.org/10.1039/d0sc06867e.
[18] M.E. Simms, M.M. Sibley, D.M. Driscoll, V. Kertesz, J.T. Damron, A.S. Ivanov, F. D. White, N.A. Thiele, Reining in radium for nuclear medicine: extra-large chelator development for an extra-large ion, Inorg. Chem. (2023), https://doi.org/10.1021/acs.inorgchem.3c02985.
[19] A. Roca-Sabio, M. Mato-Iglesias, D. Esteban-Gómez, É. Toth, A. De Bias, C. Platas-Iglesias, T. Rodríguez-Blas, Macrocyclic receptor exhibiting unprecedented selectivity for light lanthanides, J. Am. Chem. Soc. 131 (2009) 3331–3341, https://doi.org/10.1021/ja808534w.
[20] M.K. Blei, L. Waurick, F. Reissig, K. Kopka, T. Stumpf, J. Kretzschmar, C. Mamat, Equilibrium thermodynamics of macropa complexes with selected metal isotopes of radiopharmaceutical interest, Inorg. Chem. (2023), https://doi.org/10.1021/acs.inorgchem.3c01983.
[21] N.A. Thiele, S.N. Macmillan, J.J. Wilson, Rapid dissolution of $BaSO_4$ by macropa, an 18-membered macrocycle with high affinity for Ba^{2+}, J. Am. Chem. Soc. 140 (2018) 17071–17078, https://doi.org/10.1021/jacs.8b08704.
[22] N.A. Thiele, V. Brown, J.M. Kelly, A. Amor-Coarasa, U. Jermilova, S.N. MacMillan, A. Nikolopoulou, S. Ponnala, C.F. Ramogida, A.K.H. Robertson, C. Rodríguez-

Rodríguez, P. Schaffer, C. Williams, J.W. Babich, V. Radchenko, J.J. Wilson, An eighteen-membered macrocyclic ligand for actinium-225 targeted alpha therapy, Angew, Chemie Int. Ed. 56 (2017) 14712–14717, https://doi.org/10.1002/anie.201709532.
[23] E. Aluicio-Sarduy, N.A. Thiele, K.E. Martin, B.A. Vaughn, J. Devaraj, A.P. Olson, T. E. Barnhart, J.J. Wilson, E. Boros, J.W. Engle, Establishing radiolanthanum chemistry for targeted nuclear medicine applications, Chem. A Eur. J. 26 (2020) 1238–1242, https://doi.org/10.1002/chem.201905202.
[24] J.M. Kelly, A. Amor-Coarasa, S. Ponnala, A. Nikolopoulou, C. Williams, N. A. Thiele, D. Schlyer, J.J. Wilson, S.G. DiMagno, J.W. Babich, A single dose of ^{225}Ac-RPS-074 induces a complete tumor response in an LNCaP xenograft model, J. Nucl. Med. 60 (2019) 649–655, https://doi.org/10.2967/jnumed.118.219592.
[25] K. Baba, K. Nagata, T. Yajima, T. Yoshimura, Synthesis, structures, and equilibrium reactions of La(III) and Ba(II) complexes with pyridine phosphonate pendant arms on a Diaza-18-crown-6 ether, Bull. Chem. Soc. Jpn. 95 (2022) 466–475, https://doi.org/10.1246/bcsj.20210414.
[26] D.J. Fiszbein, V. Brown, N.A. Thiele, J.J. Woods, L. Wharton, S.N. Macmillan, V. Radchenko, C.F. Ramogida, J.J. Wilson, Tuning the kinetic inertness of Bi^{3+} complexes: the impact of donor atoms on Diaza-18-Crown-6 ligands as chelators for ^{213}Bi targeted alpha therapy, Inorg. Chem. 60 (2021) 9199–9211.
[27] P.L. Brown, A.V. Matyskin, C. Ekberg, The aqueous chemistry of radium, Radiochim. Acta 110 (2022) 505–513, https://doi.org/10.1515/ract-2021-1141.
[28] ADF2019, SCM, Theoretical Chemistry, Vrije Univ, Amsterdam, Netherlands, 2024. https://www.scm.com.
[29] G. te Velde, F.M. Bickelhaupt, E.J. Baerends, C. Fonseca Guerra, S.J.A. van Gisbergen, J.G. Snijders, T. Ziegler, Chemistry with ADF, J. Comput. Chem. 22 (2001) 931–967, https://doi.org/10.1002/jcc.1056.
[30] J.P. Perdew, K. Burke, M. Ernzerhof, Generalized gradient approximation made simple, Phys. Rev. Lett. 77 (1996) 3865–3868, https://doi.org/10.1103/PhysRevLett.77.3865.
[31] S. Grimme, J. Antony, S. Ehrlich, H. Krieg, A consistent and accurate ab initio parametrization of density functional dispersion correction (DFT-D) for the 94 elements H-Pu, J. Chem. Phys. 132 (2010) 154104, https://doi.org/10.1063/1.3382344.
[32] S. Grimme, Density functional theory with London dispersion corrections, Wiley Interdiscip. Rev. Comput. Mol. Sci. 1 (2011) 211–228, https://doi.org/10.1002/wcms.30.
[33] E. Van Lenthe, E.J. Baerends, J.G. Snijders, Relativistic total energy using regular approximations, J. Chem. Phys. 101 (1994) 9783–9792, https://doi.org/10.1063/1.467943.
[34] A. Klamt, G. Schüürmann, COSMO: a new approach to dielectric screening in solvents with explicit expressions for the screening energy and its gradient, J. Chem. Soc. Perkin Trans. 2 (1993) 799–805, https://doi.org/10.1039/P29930000799.
[35] C.C. Pye, T. Ziegler, An implementation of the conductor-like screening model of solvation within the Amsterdam density functional package, Theor. Chem. Accounts 101 (1999) 396–408, https://doi.org/10.1007/s002140050457.
[36] Y. Gao, E. Varathan, P. Grover, G. Schreckenbach, Computational characterization of Ac^{III}-DOTA complexes in aqueous solution, Inorg. Chem. 60 (2021) 6971–6975, https://doi.org/10.1021/acs.inorgchem.1c00254.
[37] J. Tomeček, C. Li, G. Schreckenbach, Actinium coordination chemistry: a density functional theory study with monodentate and bidentate ligands, J. Comput. Chem. 44 (2023) 334–345, https://doi.org/10.1002/jcc.26929.
[38] K. Morokuma, Why do molecules interact? The origin of electron donor-acceptor complexes, hydrogen bonding, and proton affinity, Acc. Chem. Res. 10 (1977) 294–300, https://doi.org/10.1021/ar50116a004.
[39] L.P. Wolters, F.M. Bickelhaupt, The activation strain model and molecular orbital theory, Wiley Interdiscip. Rev. Comput. Mol. Sci. 5 (2015) 324–343, https://doi.org/10.1002/wcms.1221.
[40] M. Tosato, M. Asti, M. Dalla Tiezza, L. Orian, D. Häussinger, R. Vogel, U. Köster, M. Jensen, A. Andrighetto, P. Pastore, V. Di Marco, Highly stable silver(I) complexes with cyclen-based ligands bearing sulfide arms: a step toward silver-111 labeled radiopharmaceuticals, Inorg. Chem. 59 (2020) 10907–10919.
[41] T. Scattolin, I. Pessotto, E. Cavarzerani, V. Canzonieri, L. Orian, N. Demitri, C. Schmidt, A. Casini, E. Bortolamiol, F. Visentin, F. Rizzolio, S.P. Nolan, Indenyl and allyl palladate complexes bearing N-heterocyclic carbene ligands: an easily accessible class of new anticancer drug candidates, Eur. J. Inorg. Chem. (2022) e202200103, https://doi.org/10.1002/ejic.202200103.
[42] A. Michalak, M. Mitoraj, T. Ziegler, Bond orbitals from chemical valence theory, J. Phys. Chem. A 112 (2008) 1933–1939, https://doi.org/10.1021/jp075460u.
[43] L. Zhao, M. Hermann, W.H.E. Schwarz, G. Frenking, The Lewis electron-pair bonding model: modern energy decomposition analysis, Nat. Rev. Chem. 3 (2019) 48–63, https://doi.org/10.1038/s41570-018-0060-4.
[44] M. Tosato, M. Verona, R. Doro, M. Dalla Tiezza, L. Orian, A. Andrighetto, P. Pastore, G. Marzaro, V. Di Marco, Toward novel Sulphur-containing derivatives of tetraazacyclododecane: synthesis, acid-base properties, spectroscopic characterization, DFT calculations, and cadmium(II) complex formation in aqueous solution, New J. Chem. 44 (2020) 8337–8350.
[45] Hyperquad. http://www.hyperquad.co.uk/.
[46] V. Di Marco, Studio della formazione di complessi tra alluminio e molecole di interesse ambientale, biologico e farmaceutico,, PhD Thesis,, University of Padova, 1998.
[47] A. Yamaguchi, K. Nagata, K. Kobayashi, K. Tanaka, T. Kobayashi, H. Tanida, K. Shimojo, T. Sekiguchi, Y. Kaneta, S. Matsuda, K. Yokoyama, T. Yaita, T. Yoshimura, M. Okumura, Y. Takahashi, Extended X-ray absorption fine structure spectroscopy measurements and *ab initio* molecular dynamics simulations reveal the hydration structure of the radium(II) ion, IScience 25 (2022) 104763, https://doi.org/10.1016/j.isci.2022.104763.
[48] A.V. Matyskin, N.L. Hansson, P.L. Brown, C. Ekberg, Barium and radium complexation with ethylenediaminetetraacetic acid in aqueous alkaline sodium chloride media, J. Solut. Chem. 46 (2017) 1951–1969, https://doi.org/10.1007/s10953-017-0679-7.
[49] A.V. Matyskin, P.L. Brown, C. Ekberg, Weak barium and radium hydrolysis using an ion exchange method and its uncertainty assessment, J. Chem. Thermodyn. 128 (2019) 362–371, https://doi.org/10.1016/j.jct.2018.08.037.
[50] J. Schubert, Complexes of alkaline earth cations including radium with amino acids and related compounds, J. Am. Chem. Soc. 76 (1954) 3442–3444.
[51] T. Sekine, Y. Kawashima, T. Unnai, M. Sakairi, Studies of the alkaline earth complexes in various solutions. IV. Solvent extraction study of radium(II) complexes with some aminocarboxylic acids in perchlorate media, Bull. Chem. Soc. Jpn. 41 (1968) 3013–3015.
[52] F. Nelson, R.A. Day, K.A. Kraus, Anion exchange studies-XXX a number of elements in ethylenediaminetetraacetic acid solutions, J. Inorg. Nucl. Chem. 15 (1960) 140–150, https://doi.org/10.1016/0022-1902(60)80022-X.
[53] R.G. Pearson, Hard and soft acids and bases, HSAB, part I: fundamental principles, J. Chem. Ed. 45 (1968) 581–587.
[54] V. Migliorati, A. Caruso, P. D'Angelo, Unraveling the hydration properties of the Ba^{2+} aqua ion: the interplay of quantum mechanics, molecular dynamics, and EXAFS spectroscopy, Inorg. Chem. 58 (2019) 14551–14559, https://doi.org/10.1021/acs.inorgchem.9b02204.
[55] A. Yamaguchi, K. Kobayashi, Y. Takahashi, M. Machida, M. Okumura, Hydration structures of barium ions: *ab initio* molecular dynamics simulations using the SCAN meta-GGA density functional and EXAFS spectroscopy studies, Chem. Phys. Lett. 780 (2021) 138945, https://doi.org/10.1016/j.cplett.2021.138945.